A revised model of ammonium perchlorate combustion with detailed kinetics

Pierre Bernigaud, Dmitry Davidenko, Laurent Catoire

A Revised Model of Ammonium Perchlorate Combustion with Detailed Kinetics

Pierre Bernigaud[a,†], Dmitry Davidenko[a], Laurent Catoire[b]

[a] *DMPE, ONERA, Université Paris Saclay, 91120 Palaiseau, France*
[b] *Unité Chimie et Procédés (UCP), ENSTA Paris, Institut Polytechnique de Paris, 91120 Palaiseau, France*
pierre.bernigaud@onera.fr · dmitry.davidenko@onera.fr · laurent.catoire@ensta-paris.fr
[†] Corresponding author

Abstract

In this study, we propose a revised coupled combustion model for ammonium perchlorate (AP), leveraging recent advances in the modelling of ammonia and NO_x chemistry. A coupled combustion model relies on three founding bricks: a detailed gas-phase kinetic model, a condensed-phase decomposition model, and a pyrolysis law describing the relationship between the surface temperature and mass flow. The proposed gas-phase kinetic model, is validated against data on species sampling in jet-stirred reactors, laminar flame speed, and ignition delay time. These test cases, rarely used by the solid propellant community, highlight deficiencies in a reference mechanism from the literature. A new model for AP decomposition in the condensed phase is proposed to be used with the gas-phase mechanism. A suitable pyrolysis law is designed using the Zel'dovich-Novozhilov theory to ensure the stability of the coupled combustion model. The methodology employed is described in detail, for others to replicate. Finally, the overall model is applied to simulate the AP laminar flame in a 1D coupled approach. These calculations provide results on the regression rate, surface temperature, temperature sensitivity and species profiles for prescribed initial temperature of AP and ambient pressure. The behavior of the proposed combustion model is presented in comparison with other reference models. The role of gas-phase kinetics in modeling AP combustion is discussed.

Keywords: Ammonium perchlorate; kinetic mechanism, pyrolysis law; coupled flame/solid simulation

1. Novelty and Significance

Current models for ammonium perchlorate (AP) combustion have been used for more than a decade without significant revision or improvement. Furthermore, all of these models have been validated primarily on a dataset limited to AP combustion with a unique case of detailed flame structure. By applying a more rigorous methodology, the validation dataset is expanded adding cases on simple reactive systems of interest. This approach highlights fundamental deficiencies in the mechanisms which were widely used in the past. A new gas-phase kinetic mechanism with improved confidence is assembled and validated on the expanded dataset. A condensed-phase decomposition model is formulated to be used conjointly. Finally, a pyrolysis law is designed employing the Zel'dovich-Novozhilov theory of solid propellant combustion stability and optimizing the Arrhenius parameters.

2. Authors Contributions

P. B. performed research, wrote the paper.
D. D. supervised research, wrote the paper.
L. C. supervised research.

3. Introduction

Ammonium perchlorate combined with a polymeric binder such as hydroxytelechelic polybutadiene (HTPB) is a widely used ingredient for composite solid propellants. These composite propellants are used for both civilian and military applications. While the binder provides the combustible gases via its pyrolysis, the AP acts as a source of oxidizer. The combustion process is controlled by the modal distribution of the AP particles in the propellant. A composite propellant can be tailored to meet specific requirements using appropriate AP loading.
In order to design a composite propellant, it is important to understand and properly model the combustion of pure AP. To this end, it is necessary to develop a detailed chemical kinetic mechanism in the gas phase and a model of AP decomposition in the condensed phase.
Extensive experimental work has been carried out in the past, the results of which are essential for the construction and validation of numerical models. The models must first verify the macroscopic characteristics of the AP combustion: Atwood and Boggs [1] measured the regression rate of AP at various pressures, as well as the initial temperature sensitivity. Surface temperature measurements were performed by Bakhman et al. [2], Powling et al. [3], and Korobeinichev et al. [4]. The combustion model must also represent the underlying chemical mechanisms within the flame. To this end, the work of Ermolin et al. [5] provides chemical species profiles in an AP flame at low pressure. For this same flame, Tereshenko et al. [6] reported measurements of the temperature profile near the regression surface. On this experimental base, Ermolin et al. [5] proposed a first chemical kinetic mechanism in the gas phase, able to reproduce satisfactorily the measured species profiles. Tanaka et al. [7] then Jing et al. [8] presented models coupling the gas-phase combustion and condensed-phase decomposition processes. The inclusion of the condensed phase has improved the macroscopic performance of the model (prediction of burning rate, temperature sensitivity). Efforts to develop more accurate combustion models for AP were continued by Meynet et al. [9], Gross et al. [10] and Smyth et al. [11].
Ammonium perchlorate (NH_3HClO_4) decomposes in the condensed phase via different pathways, the most important of them forming NH_3 and $HClO_4$. The presence of NH_3 among the main decomposition products requires an appropriate kinetic model for NH_3, its subsequent radicals, and NO_x. Chemical experiments involving ammonia have been numerically reproduced with the model used by Gross et al. [10], highlighting some important deficiencies.
Based on this finding, we first propose a new gas-phase kinetic model for AP combustion based on the recent work on ammonia oxidation from Shrestha et al. [12]. A revised model of the condensed-phase decomposition process is then formulated to be coupled to the new gas-phase kinetic mechanism. The relation between the regression rate and the surface temperature is specified via an adapted pyrolysis law. Simulations of AP combustion using a coupled flame/solid approach are performed to evaluate several macroscopic parameters (burning rate, surface temperature), serving as validation criteria with respect to the available experimental data. Temperature and chemical species profiles are computed for the low-pressure flame studied by Ermolin et al. [5] and Tereshenko et al. [6]. Finally, a stability study is carried out, in the sense of the Zel'dovich-Novozhilov theory [13].

4. Gas Phase Mechanism

The proposed mechanism for AP combustion consists of 36 species and 205 reactions. It contains sub-mechanisms for the H-O system, nitrogen-containing species, and chlorinated species. This model was developed based on the work of Shrestha et al. [12] on ammonia combustion for the H-O-N part of the mechanism. This reference model is hereafter called the Shrestha model. The choice of this specific mechanism for the reactions involving NH_3 and

other nitrogen-containing species is based on its validation against a large data-set. It is to be noted that ammonia combustion is still a very active field of research, and more recent mechanisms can be found, see Shrestha et al. [14], Baker et al. [15] . The sub-mechanism for chlorinated species is inspired by the work of Smooke and Yetter [16], itself based on the historic mechanism proposed by Ermolin et al. [17]. This last sub-mechanism also includes reactions used by Pelucchi et al. [18] in his study of the HCl/Cl_2 chemistry at high temperature. The proposed mechanism is available in the supplementary materials.

In the following subsections, the ability of the mechanism to accurately represent the NH_3/O_2 chemistry is first validated via laminar flame speed and ignition delay calculations. The $H_2/O_2/NO_x$ chemistry is tested on experiments in a jet-stirred reactor and a shock tube. The correct treatment of the Cl_2/H_2 chemistry is also verified via laminar flame speed and ignition delay calculations. The test cases are selected from the works of Shrestha et al. [12] and Pelucchi et al. [18]. This is to ensure that the performance of the assembled AP kinetic model is similar to the original mechanisms from [12, 18]. The results presented below serve to demonstrate AP model improvements with respect to existing AP mechanisms, and not to provide an exhaustive validation. The new mechanism is compared to the reference model proposed by Gross et al. [10], hereafter called the Gross model (25 species, 80 reactions). This specific model is chosen as a reference, owing to its frequent usage within the solid propellant community.

Chemical experiments are simulated employing the Cantera software [19]. Laminar flame speed is obtained under the hypothesis of adiabatic combustion. Jet-stirred reactors are modeled as perfectly-stirred reactors. In order to assess the performance of a given kinetic model, we use the adimensional L_2 error norm:

$$\delta_{err} = \frac{1}{\mu_y}\left[\sum_{k=1}^{N}(y_k - \hat{y}_k)^2\right]^{\frac{1}{2}} \tag{1}$$

Where N is the number of experimental data points, the k-th data point is (x_k, y_k), $\hat{y}_k$ is the estimate produced by a model at x_k, and μ_y is the average value of the experimental data points. For ignition delay experiments, the log-ratio measure is used to better represent the large range of time scales within the data:

$$\delta_{err} = \left[\sum_{k=1}^{N}\left(\log\frac{y_k}{\hat{y}_k}\right)^2\right]^{\frac{1}{2}} \tag{2}$$

Where log is the decimal logarithm.

4.1. NH_3 / O_2 *Chemistry*

Ammonia (NH_3) is one of the main decomposition products of ammonium perchlorate. In order to validate the oxidation sub-mechanism of NH_3, different experiments are reproduced with the present model. The ignition delay time for a highly diluted NH_3/O_2 mixture is calculated for various pressure and equivalence ratio. The results are compared in Figure 1 with the measurements in shock-tube experiments by Mathieu et al. [20]. The error between the model predictions and experimental data is quantified in Table 1.

Table 1: Ignition delay time for NH_3/O_2 mixtures: error norm of the model predictions.

ϕ	P (atm)	δ_{err}
0.5	1.4	$2.69 \cdot 10^{-1}$
0.5	11	$1.94 \cdot 10^{-1}$
0.5	30	$1.48 \cdot 10^{-1}$
1	1.4	$3.55 \cdot 10^{-1}$
1	11	$2.07 \cdot 10^{-1}$
1	30	$1.95 \cdot 10^{-1}$

Good agreement between the model predictions and the experimental results is achieved. Results obtained with the Gross model [10] are not reported: no ignition was observed with it. Indeed, this model has no reaction between NH_3 and O_2, nor dissociation reaction for these species. The ignition is initiated in the present mechanism via reactions R92 and R97:

$$NH_3 + M = NH_2 + H + M \tag{R92}$$

$$NH_3 + O_2 = HO_2 + NH_2 \tag{R97}$$

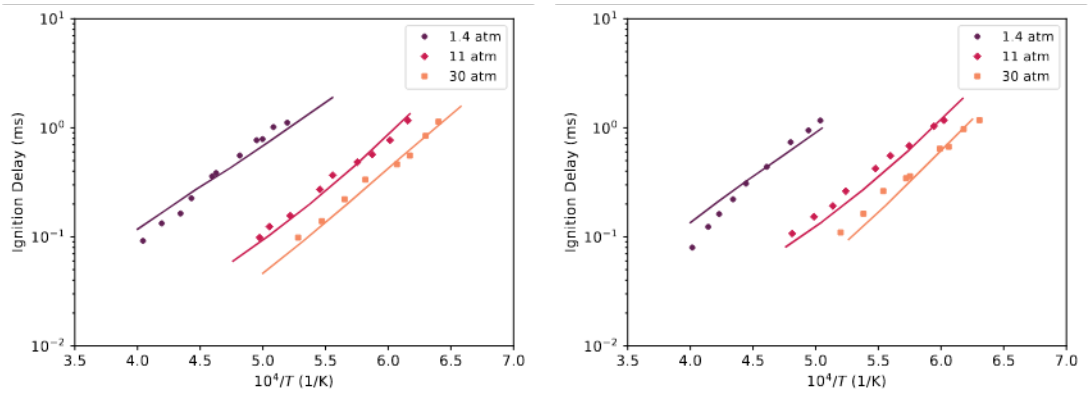

(a) $\Phi = 0.5$ (b) $\Phi = 1$

Fig. 1: Ignition delay time of NH_3/O_2 mixtures for various pressure (1.4, 11 and 30 atm) and equivalence ratio ($\phi = 0.5$ and 1), initial temperature 298 K. Symbols: experiment [20]. Lines: model predictions.

Reaction R92 is particularly important. It produces hydrogen atoms, which participate in the formation of the OH and O radicals via the following reaction:

$$H + O_2 = OH + O \tag{R5}$$

The ammonia NH_3 is then transformed into NH_2 by reactions with O, H and OH radicals:

$$NH_3 + O = NH_2 + OH \tag{R93}$$
$$NH_3 + H = NH_2 + H_2 \tag{R94}$$
$$NH_3 + OH = NH_2 + H_2O \tag{R95}$$

Reactions R93 and R94 consume the majority of NH_3. NH_2 is then converted via two paths, forming NH and N_2H_2 respectively:

$$NH_2 + H = NH + H_2 \tag{R79}$$
$$NH_2 + O = NH + OH \tag{R78}$$
$$NH_2 + NH = N_2H_2 + H \tag{R73}$$
$$NH_2 + NH_2 = N_2H_2 + H_2 \tag{R90}$$

The final product N_2 is mainly formed from N_2H_2 via the intermediary NNH:

$$N_2H_2 + M = NNH + H + M \tag{R108}$$
$$NNH + M = N_2 + H + M \tag{R100}$$

Several hydrogen-abstraction reactions involving NH_x produce H_2, which is finally converted into H_2O via:

$$OH + H_2 = H_2O + H \tag{R8}$$

The predicted laminar flame speeds for the NH_3 / air system at 1 atm are presented in Figure 2a and compared with available experimental data. Are also reported the predictions obtained with the Gross reference model [10] and the Shrestha model [12] that served for the development of the present work. The error norm related to each model is presented in Table 2.
Good agreement is found between the predictions of the present model and the experimental results. The Gross model [10] over predicts the flame speed, especially at lower equivalence ratios but captures the velocity maximum

Table 2: Laminar flame speed for NH_3/ air mixtures at 1 atm: error norm of the model predictions.

Model	δ_{err}
This work	$1.94 \cdot 10^0$
Shrestha [12]	$2.07 \cdot 10^0$
Gross [10]	$2.14 \cdot 10^1$

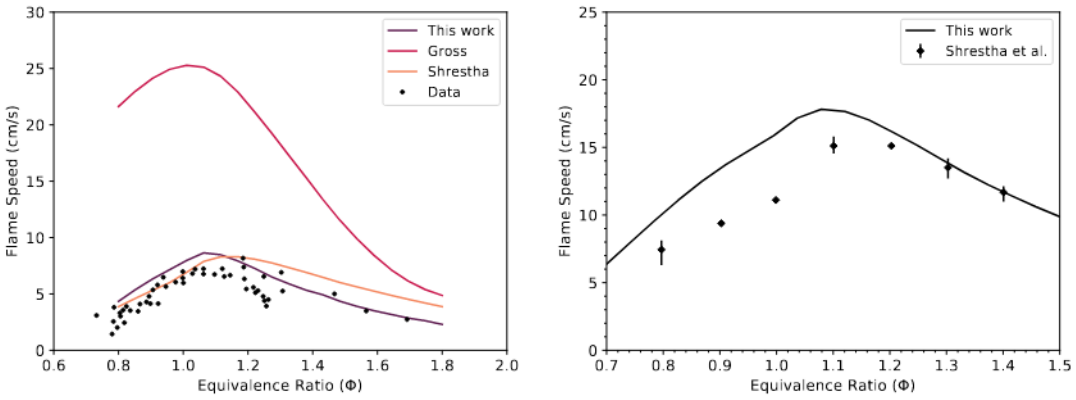

(a) Pressure 1 atm.

(b) Pressure 3 atm.

Fig. 2: Laminar flame speed versus equivalence ratio for NH_3/air mixtures at 298 K and for two pressures. Symbols: experiments. (a) [21–26], (b) [14]. Lines: Model predictions.

around stoichiometry. It may be noted that the present mechanism performs better than the Shrestha model [12] for rich conditions, where the slope defined by the experimental points is well followed. To test the mechanism at a higher pressure, the laminar flame speed for the NH_3 / air system is computed at 3 atm, Figure 2b. The modelling results are good for rich conditions, but somewhat higher than the experimental data under lean conditions. Experimental work is still required to obtain data at high pressures, which correspond to the AP combustion conditions in solid rocket motors.

A sensitivity analysis is performed on this laminar flame case, for 1 atm. We define the sensitivity coefficient σ_k for reaction k via:

$$\sigma_k = \frac{\partial \ln (S_L)}{\partial \ln (\delta_k)} \tag{3}$$

Where S_L is the laminar flame speed and δ_k a perturbation applied to the pre-exponential factor of the reaction k. This coefficient is calculated for rich ($\phi = 1.8$) and lean ($\phi = 0.8$) conditions, and the reactions of the highest sensitivity are reported in Figure 3.

It can be noted that for both considered equivalence ratios, the branching reaction R5 has the highest sensitivity.

$$H + O_2 = OH + O \tag{R5}$$

The chemistry of N_2H_2 is also important in rich and lean environments. We notice that reaction R125 has adverse effects under lean and rich conditions.

$$N_2H_3 + NH_2 = N_2H_2 + NH_3 \tag{R125}$$

Reactions involving NO_x have particular sensitivity when fuel is lacking, and little effect in rich mixtures.

$$NH + O_2 = HNO + O \tag{R61}$$
$$NH_2 + NO = NNH + OH \tag{R82}$$
$$NH + NO = H + N_2O \tag{R68}$$
$$H + N_2O = N_2 + OH \tag{R58}$$
$$NH_2 + NO = H_2O + N_2 \tag{R83}$$

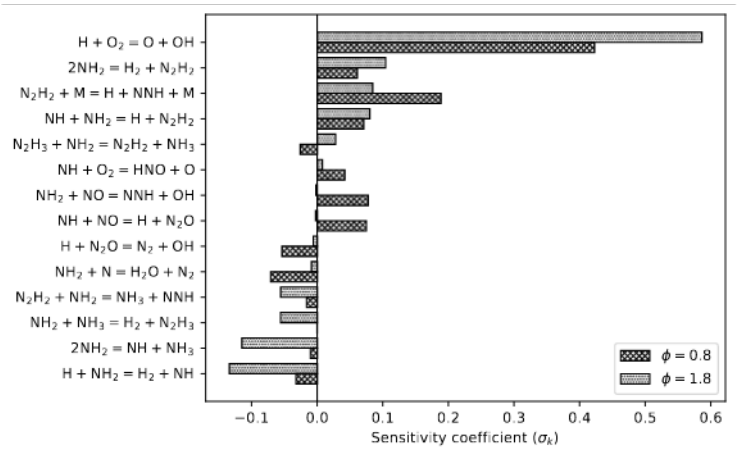

Fig. 3: Sensitivity coefficient for the laminar flame speed of the NH_3 / air system, at 1 atm and two equivalence ratios.

Finally, the reactions involving NH_x, such as R79, R87 and R99, are important in rich mixtures and less significant in lean environment.

$$H + NH_2 = H_2 + NH \quad \text{(R79)}$$

$$NH_2 + NH_2 = NH + NH_3 \quad \text{(R87)}$$

$$NH_2 + NH_3 = H_2 + N_2H_3 \quad \text{(R99)}$$

More generally, we observe a notable variation of the reaction sensitivity with the equivalence ratio.

4.2. $H_2/O_2/NO_x$ Chemistry

Combustion of ammonium perchlorate leads to production of various NO_x species. It is therefore important to ensure the validity of the kinetics involving these species. The $H_2/O_2/NO_x$ sub-mechanism in validated on experiments in a jet-stirred reactor. The first test case, Figure 4, corresponds to a mixture of reactants H_2 (1%) / O_2 (1%) / N_2 doped with 220 ppm of NO. The pressure is 10 atm and the residence time is 1s.

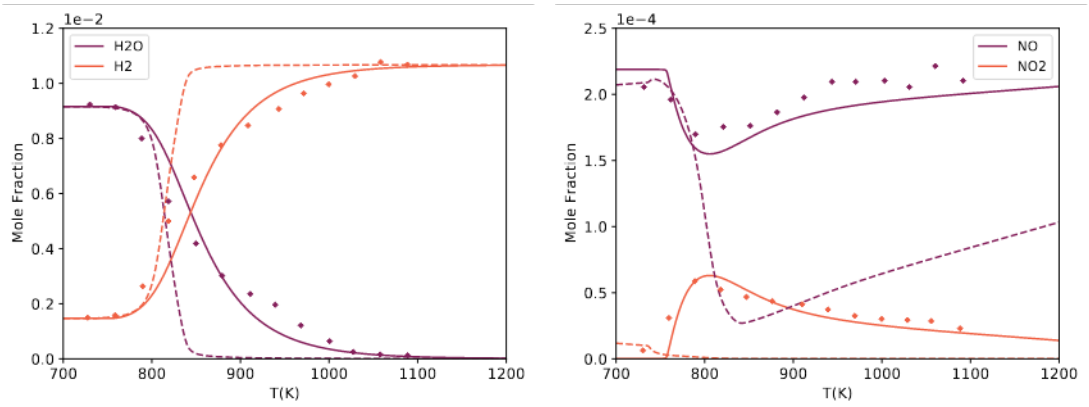

Fig. 4: Products in a jet-stirred reactor of the mixture H_2 (1%) / O_2 (1%) / N_2 with NO (220 ppm) at 10 atm, residence time 1 s, variable temperature. Symbols: experiment [27]. Solid lines: present model. Dashed lines: Gross model

.

The Gross model [10] predicts correctly the crossover temperature of the H_2 and H_2O curves, around 825 K, but the results deviate rapidly from the experimental points as the temperature increases. The present model provides satisfactory results for the nitrogen-containing species. The crossover temperature is slightly over-predicted. The reaction is initiated by:

$$H_2 + O_2 = HO_2 + H \quad \text{(R11)}$$

H_2 is then converted into H_2O via:

$$OH + H_2 = H_2O + H \quad \text{(R8)}$$

The rate of consumption of H_2 is therefore controlled by the concentration of OH in the gas. Three pathways forming OH are identified:

$$H + O_2 = O + OH \quad \text{(R5)}$$
$$NO_2 + H = NO + OH \quad \text{(R44)}$$
$$NO + HO_2 = NO_2 + OH \quad \text{(R46)}$$

At low temperature (700 K), these three reactions are almost inactive, prohibiting the conversion of H_2 to H_2O. At 850 K, reaction R46 is particularly active: we observe conversion from NO to NO_2 and acceleration of the hydrogen chemistry. At higher temperatures, reactions R5 and R46 are more active, reforming NO from NO_2. In the Gross model, reaction R46 is absent, which explains why the NO to NO_2 conversion process is not observed. At 850 K, reactions R5 and R44 are very active: OH is produced in large quantities and the oxidation of H_2 is strongly accelerated. The drop in the NO level is explained by its conversion via HNO into NO_2, which is readily transformed into OH via R44 to accelerate the H_2 oxidation.

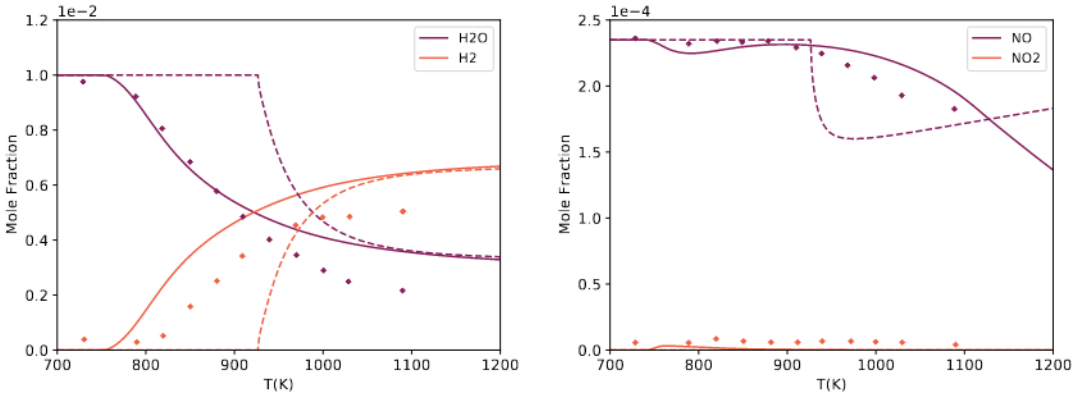

Fig. 5: Products in a jet-stirred reactor of the mixture H_2 (1%) / O_2 (0.333%) / N_2 doped with NO (235 ppm) at 1 atm, residence time 0.24 s, variable temperature. Symbols: experiment [27]. Solid lines: present model. Dashed lines: Gross model [10].

A similar case with a lower pressure (1 atm) and a higher equivalence ratio ($\Phi = 1.5$) is presented in Figure 5. The profiles obtained with the present model for nitrogen-containing species are satisfactory. For H_2 and H_2O, the prediction is consistent with the results presented by Shrestha et al. [12]. The H_2 oxidation is again controlled by the production of OH. At low temperature (800 K), OH is produced via R44 and R46. These two reactions progress in the forward direction. Their balance is essential to ensure production of OH allowing the oxidation H_2 at a correct rate, to avoid over-consuming or over-producing NO and NO_2. The action of these two reactions is less important at lower temperatures compared to the conversion phenomenon observed in Figure 4. At higher temperatures, they contribute to the consumption of NO, explaining the decrease in the NO level observed around 1000K. As in the previous case, the Gross model presents a significant drop in the NO level which abruptly accelerates the oxidation of H_2. However, the onset of this process occurs at a much higher temperature than in the experiment.

Another case, presented in Figure 6, is to study the effect of NO_2 as a doping species. A similar reactive mixture as in the previous case is doped with 60 ppm of NO_2 at 10 atm. For both models the H_2 to H_2O conversion is predicted satisfactorily, the NO_2 to NO conversion takes place via the reaction $NO_2 + H = NO + OH$. In the Gross model, this reaction is too rapid, causing an overproduction of NO at low temperature; NO formed is then rapidly converted into N_2 via the reaction $NO + HNO = N_2 + HO_2$ resulting in the low NO level at high temperature. This last reaction is absent in the new model, providing a closer agreement with the experimentally measured NO level.

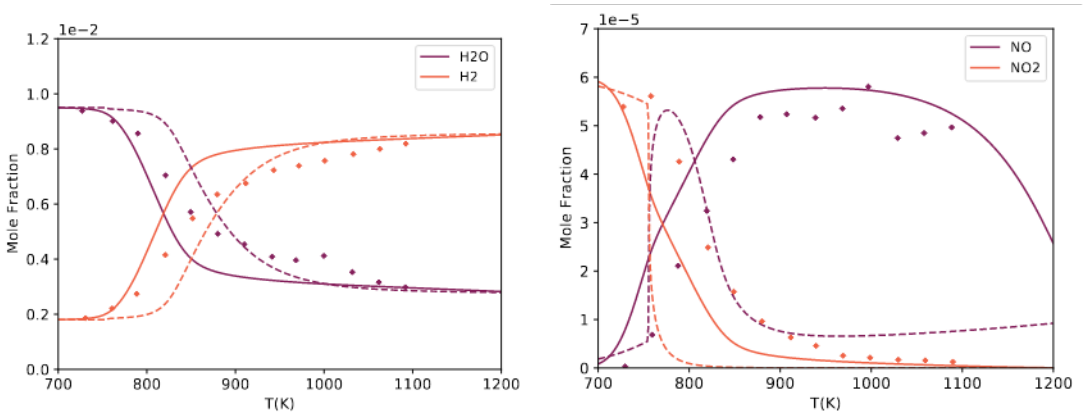

Fig. 6: Products in a jet-stirred reactor of the mixture H_2 (1%) / O_2 (0.333%) / N_2 doped with NO_2 (60 ppm) at 10 atm, 1 s residence time, variable temperature. Symbols: experiment [27]. Solid lines: present model. Dashed lines: Gross model [10].

The kinetic model is finally tested on a self-ignition case, for a H_2 (1%)/O_2(1%)/Ar mixture with 100 ppm of NO_2 at various pressures (1.7, 13. and 33. atm), Figure 7. For the lowest pressure, the model predictions follow the linear trend, corresponding to the ignition regime controlled by the chain branching mechanism. However, the predicted transition due to chain termination at lower temperature or higher pressures is shifted to the left of the experimental points. The Gross model largely overpredicts the ignition delay time at all pressures.

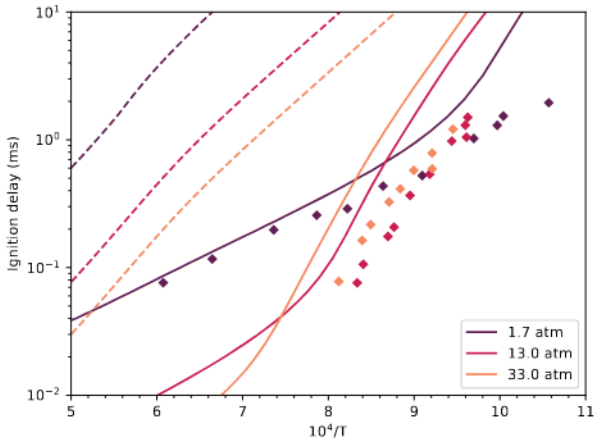

Fig. 7: Ignition delay time of a H_2 (1%)/O_2(1%)/Ar mixture with NO_2 (100 ppm) for various pressures (1.7, 13 and 33 atm), initial temperature 298 K. Symbols: experiment [28]. Solid lines: present model. Dashed lines: Gross model [10].

4.3. Cl_2 / H_2 Chemistry

The experimental and modeling results on the ignition delay time for different Cl_2 / H_2 / Ar mixtures are reported in Figure 8. The experimental points come from measurements made by Lifshitz and Schechner [29] in a shock tube over the temperature range 830 K to 1260 K. The cases considered are grouped in Table 3. The mole fractions shown represent the initial composition of the reactive mixture, P_1 is the initial pressure, and P_5 is the pressure after the reflected shock.

Cases A and B demonstrate the ability of the models to reproduce the effect of pressure on the ignition delay time for a stoichiometric mixture. Cases C, D, and E allow testing the effect of equivalence ratio at a constant pressure. Good agreement between the model curves and experimental points is observed for these cases at higher temperatures, but discrepancies increase at lower temperatures, particularly for cases C and E. In general, the present model produces systematically better predictions than the Gross model.

As reported by Pelucchi et al. [18], the ignition delay is mainly controlled by the R159 initiation reaction and the R163 branching reaction forming Cl and H radicals.

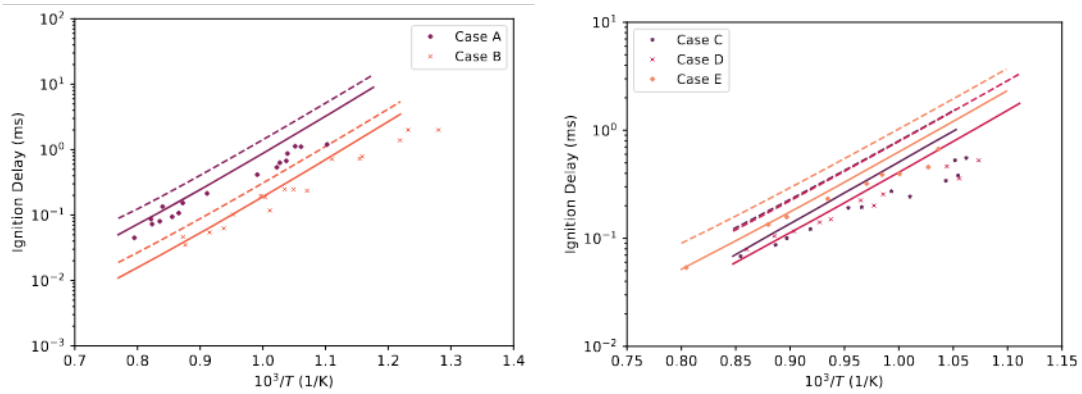

Fig. 8: Ignition delay time for Cl_2/H_2/Ar mixtures. Cases are presented in Table 3. Symbols: experiment [29]. Solid lines: present model. Dashed lines: Gross model.

Table 3: Conditions for ignition modelling in Cl_2/H_2/Ar mixtures and error norm of the model predictions.

Case	Cl_2 (%)	H_2 (%)	P_1 (atm)	P_5 (atm)	δ_{err} Gross	δ_{err} This work
A	10.4	10.4	0.066	1.0	$1.79 \cdot 10^0$	$9.83 \cdot 10^{-1}$
B	10.4	10.4	0.263	4.6	$1.49 \cdot 10^0$	$8.19 \cdot 10^{-1}$
C	19.8	10.0	0.066	1.3	$1.38 \cdot 10^0$	$7.74 \cdot 10^{-1}$
D	10.3	21.6	0.066	1.3	$1.42 \cdot 10^0$	$5.99 \cdot 10^{-1}$
E	11.0	11.0	0.066	1.3	$1.06 \cdot 10^0$	$4.71 \cdot 10^{-1}$

$$Cl_2 + M = Cl + Cl + M \quad \text{(R159)}$$
$$Cl + H_2 = HCl + H \quad \text{(R163)}$$

A more detailed analysis of the reaction kinetics could allow an improvement of the model predictions. The good performance observed at high temperature remains however sufficient for the combustion model of ammonium perchlorate.

The models are further validated on test cases of laminar flame speed for a Cl_2 / H_2 / N_2 mixture with different dilution levels, for which the results are shown in Figure 9. Deviations with respect to experimental data are presented in Table 4.

Table 4: Laminar flame speed for $Cl_2/H_2/N_2$ mixtures: error norm of the model predictions.

X_{N_2}	δ_{err} Gross	δ_{err} This work
0.5	$5.91 \cdot 10^{-1}$	$2.96 \cdot 10^{-1}$
0.55	$1.89 \cdot 10^0$	$1.62 \cdot 10^{-1}$
0.6	$3.78 \cdot 10^{-1}$	$1.38 \cdot 10^{-1}$

Good agreement is found between the experimental points and the predictions obtained with the present model. For the Gross model, the laminar flame speed is systematically underestimated. This defect increases for more concentrated mixtures. A sensitivity study is performed for a N_2 mole fraction of 0.5 to highlight the reactions controlling the Cl_2/H_2 chemistry, Figure 10. As for the ignition delay cases, the initiation reaction R159 and the branching reaction R163 have particular sensitivity in both rich and lean environments.

We notice that the sensitivity coefficient of the other reactions is much lower and varies significantly with the equivalence ratio. The reactions producing HCl other than the R163 pathway are:

$$Cl_2 + H = Cl + HCl \quad \text{(R162)}$$
$$Cl + H + M = HCl + M \quad \text{(R164)}$$

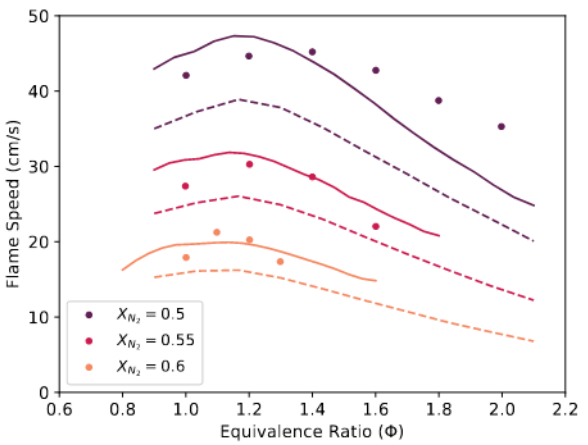

Fig. 9: Laminar flame speed for $Cl_2/H_2/N_2$ mixtures at 1 atm,298 K, and different mole fractions of N_2. Symbols: experiment [30]. Solid lines: present model. Dashed lines: Gross model [10].

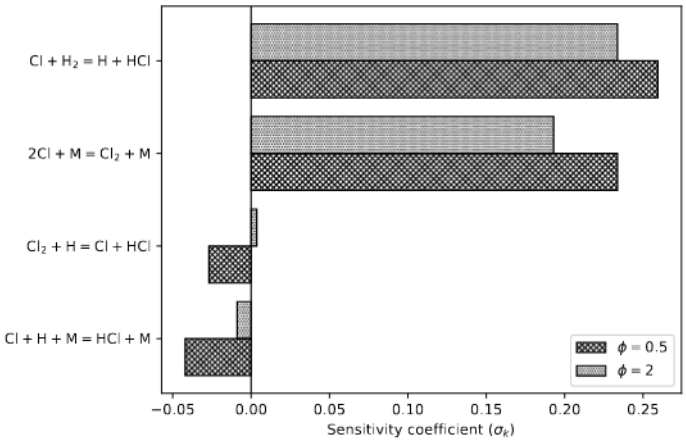

Fig. 10: Sensitivity coefficients of the laminar flame speed for $Cl_2/H_2/N_2$ mixtures at 1 atm, containing 50% of N_2, in rich ($\phi = 2$) and lean ($\phi = 0.5$) environments.

These reactions have a relatively low sensitivity coefficient. They consume H radicals and have higher sensitivity at low equivalence ratio, when there are more Cl_2 and Cl atoms in the reacting mixture. Reaction R162 consumes H radicals but also produces Cl atoms needed for reaction R163, similar to the initiation reaction R159 ; its sensitivity coefficient is thus slightly positive in rich medium, when the mixture is at lack of Cl.

As a final comment on the sub-mechanism for chlorinated species, it is to be noted that one of the main products of AP decomposition is perchloric acid $HClO_4$. The breakup of this molecule is hence an important step in the AP combustion process. The reactions modeling this step are taken from the historical mechanism of Ermolin et al. [17]. Kinetic studies of this particular molecule could greatly help the development of future combustion models for AP.

5. Coupled Combustion Model

The new gas-phase kinetic mechanism is applied to the case of ammonium perchlorate combustion. Calculations are performed in a coupled approach with the condensed phase. A diagram of the simulation domain is presented in Figure 11, showing schematically the temperature profile and phase transformation. The gas and condensed phases are considered to be separated by a planar and infinitely thin interface, for which the coupling conditions are formulated. The combustion process is assumed to be one-dimensional and steady-state in the reference frame attached to the interface. This is a usual approach for modelling solid monopropellant combustion, see Rahman et al. [31].

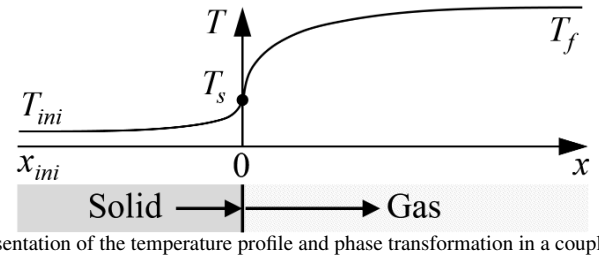

Fig. 11: Schematic representation of the temperature profile and phase transformation in a coupled combustion simulation

5.1. Governing Equations

5.1.1. Gas Phase

The governing equations for a reactive flow are formulated under the assumption of low Mach number. In the following expressions, index "g" designates bulk properties of the gas-phase and index "k" identifies the k-th chemical species.

The continuity equation is expressed as:

$$\frac{\mathrm{d}}{\mathrm{d}x}\left(\rho_g u\right) = 0 \tag{4}$$

Where ρ_g is the bulk density and u is the flow velocity. The gas density is determined as a function of the temperature and chemical species fractions for a given thermodynamic pressure. We then introduce the mass flux $m = \rho_g u$, constant in space. Under the adopted assumptions, the velocity is entirely defined by the continuity equation. The momentum equation allows obtaining the variation of the hydrodynamic pressure, which is not of interest to this problem. The equation for the mass fraction Y_k of chemical species is :

$$m\frac{\mathrm{d}Y_k}{\mathrm{d}x} = -\frac{\mathrm{d}}{\mathrm{d}x}\left(\rho_g Y_k V_k\right) + \mathcal{M}_k\dot{\omega}_k \tag{5}$$

With $\mathcal{M}_k$ the species molar mass, $\dot{\omega}_k$ its molar production rate and V_k its diffusion velocity. Finally, the energy equation is expressed as:

$$\begin{cases} m\dfrac{\mathrm{d}h_g}{\mathrm{d}x} = \dfrac{\mathrm{d}Q_g}{\mathrm{d}x} \\ Q_g = \lambda_g\dfrac{\mathrm{d}T}{\mathrm{d}x} - \rho_g\displaystyle\sum_{k=1}^{N_s} h_k Y_k V_k \end{cases} \tag{6}$$

Where T is the temperature, λ_g is the thermal conductivity, h_g and h_k are the mass-specific enthalpies.

These equations are discretized by the finite volume method and solved by a Newton-Raphson algorithm. In order to facilitate the convergence, temporal terms are introduced and discretized using the backward Euler scheme. The inlet conditions are determined by the coupling equations with the condensed phase. The gradients of T and Y_k are assumed to be zero at the outlet boundary. The CHEMKIN library [32] is used for computing the reaction rates and thermodynamic properties in the gas phase. Molecular transport properties (thermal conductivity, diffusion coefficients) are evaluated employing the EGLib library [33, 34].

5.1.2. Condensed Phase

The condensed phase properties are designated by index "c". By analogy with the gas-phase, the mass flux in the condensed phase is $m = \rho_c u$, where ρ_c is the corresponding density.

The energy equation is:

$$\begin{cases} m\dfrac{\mathrm{d}h_c}{\mathrm{d}x} = \dfrac{\mathrm{d}Q_c}{\mathrm{d}x} \\ Q_c = \lambda_c\dfrac{\mathrm{d}T}{\mathrm{d}x} \end{cases} \tag{7}$$

Where h_c is the enthalpy, and λ_c is the thermal conductivity. This equation can be expressed as two ordinary differential equations:

$$\begin{cases} \dfrac{\mathrm{d}T}{\mathrm{d}x} = \nabla T \\ \dfrac{\mathrm{d}}{\mathrm{d}x}\left(\lambda_c\nabla T\right) = mc_c\nabla T \end{cases} \tag{8}$$

With c_c the mass-specific heat capacity of the condensed phase. These equations are integrated using the DASSL algorithm [35], from the initial conditions:

$$\begin{cases} T\left(x_{\text{ini}}\right) = T_{\text{ini}} \\ \left(\lambda_c \nabla T\right)_{\text{ini}} = m\left[h_c\left(T_{\text{ini}}\right) - h_c\left(T_0\right)\right] \end{cases} \tag{9}$$

With T_0 the initial temperature of the condensed phase. The thermophysical properties of the AP are defined as dependent on the temperature and its physical state. Table 5 presents the model parameters for the solid and liquid AP. The transition enthalpy from the solid to liquid state accounts for the transition enthalpy from the orthorhombic to cubic crystalline phase of AP.

Table 5: Thermophysical properties of AP

Property	Solid AP	Liquid AP	Ref
Density ($\mathrm{kg/m^3}$)	1957	1756	[7]
Enthalpy at 298.15 K ($\mathrm{J\,kg^{-1}}$)	-2517423	-	[36]
Melting Temperature (K)	735	-	[11]
Transition Enthalpy ($\mathrm{J\,kg^{-1}}$)	-	338312	[36], [7]
Thermal Capacity ($\mathrm{J\,kg^{-1}\,K^{-1}}$)	$584.35 + 1.7054T$	1913	[37], [11]
Thermal Conductivity ($\mathrm{W\,m^{-1}\,K^{-1}}$)	$0.642 - 3.849 \cdot 10^{-4}T$	$0.416 - 1.569 \cdot 10^{-4}T$	[37], [11]

5.2. Interface Conditions

The interface between the condensed and gas phases is a particular zone to model, owing to the complexity of the physical phenomena involved. A chemically reactive foam is found in this zone. The mass and heat transfer is accompanied by decomposition reactions in the condensed phase. Few experimental results are available to model these mechanisms. The study of this interface is difficult due to its small thickness: Boggs et al. [38] reports a thickness of 1 to 5 μm, while Tanaka and Beckstead [7] estimate a thickness of less than 1 μm. It is proposed for the present modeling approach to consider this interface as an infinitely thin surface with appropriate conditions that are part of the present model. These conditions must ensure the transfer of mass, heat and species between the two phases while representing the chemical reactions taking place in the foam in a global sens.

5.2.1. Interface Chemistry

AP decomposition is represented by surface reactions. It is commonly assumed [10, 31, 39], that AP decomposes via two competing pathways. The first one is endothermic and results from direct sublimation of AP molecules via proton transfer and desorption:

$$\mathrm{AP} \rightarrow \mathrm{NH_3} + \mathrm{HClO_4} \tag{10}$$

The second exothermic pathway, forming N chemical species and hereafter called "decomposition path", is meant to model the remaining chemical reactions:

$$\mathrm{AP} \rightarrow \sum_{k=1}^{N} \nu_k \chi_k \tag{11}$$

Where χ_k designates the k-th product species and ν_k its stoichiometric coefficient. Numerous variants have been proposed for this pathway by several authors [7, 10, 11]. These models produce unsatisfactory results when coupled with the gas-phase reaction mechanism presented above. A new formulation is therefore proposed to be used in the present model:

$$\mathrm{AP} \rightarrow \frac{7}{26}\mathrm{N_2} + \frac{23}{26}\mathrm{O_2} + \frac{46}{26}\mathrm{H_2O} + \frac{7}{26}\mathrm{Cl_2} + \frac{12}{26}\mathrm{HCl} + \frac{4}{26}\mathrm{NO_2} + \frac{4}{26}\mathrm{N_2O} \tag{12}$$

The relative importance of the two pathways is controlled by parameter α, such that the global reaction including both pathways can be written as:

$$\mathrm{AP} \rightarrow \alpha\left(\mathrm{NH_3} + \mathrm{HClO_4}\right) + (1-\alpha)\sum_{k=1}^{N} \nu_k \chi_k = \sum_{k=1}^{\hat{N}} \hat{\nu}_k \chi_k, \tag{13}$$

where we introduce $\hat{\nu}_k$ the stoichiometric coefficient of species k. Since the sublimation and decomposition paths are respectively endothermic and exothermic, the α parameter has a first-order effect on the regression rate

predicted by the present model: the massflow rate increases as the value of α decreases. It is assumed in this study that α is independent of the ambient pressure and initial temperature of AP. It is fixed at a value of 0.65 to reproduce the experimentally observed evolution of the regression rate as a function of the pressure. The regression mass flux m depends on the molar consumption rate of AP at the interface, $\hat{\omega}_{\text{AP}}$, which is related to the surface temperature via a pyrolysis law, Equation (14). Its parameters, specified in Table 6, are determined from a specific study detailed in Section 6.

$$m = -\mathcal{M}_{\text{AP}}\hat{\omega}_{\text{AP}} = A\exp\left(\frac{-T_a}{T_s}\right) \tag{14}$$

Table 6: Parameters for the AP pyrolysis law

Parameter	Value
$\mathcal{M}_{\text{AP}}$ (kg mol^{-1})	0.11748
T_a (K)	7500
A ($\text{kg/m}^2\text{/s}$)	$3.0 \cdot 10^4$

5.2.2. Flux Conservation

We introduce the notation $[\cdot]$ such that:

$$[X] = X_g^I - X_c^I \tag{15}$$

Where X_c^I and X_g^I are quantities representing the boundary conditions for the condensed and gaseous phases. The interface is infinitely thin and is assumed to contain no source of mass or energy. The conservation of mass and energy fluxes across the interface leads to:

$$[m] = [\rho u] = 0 \tag{16}$$

$$[mh - Q] = 0 \tag{17}$$

The mass flux of species k in the gas phase is expressed at the interface as:

$$mY_k^I + (\rho_g Y_k V_k)^I = -\mathcal{M}_k \hat{\nu}_k \hat{\omega}_{\text{AP}} \tag{18}$$

We also impose the continuity of the temperature profile:

$$T_g^I = T_c^I = T_s \tag{19}$$

5.3. Solution Method for the Coupled Problem

Two one-dimensional physical domains are considered, for the condensed and gaseous phases. In order to ensure a correct coupling, a global iterative algorithm is employed to find the mass flow verifying the interface conditions. The residual defined by Equation must disappear through these iterations. At each global iteration, the solution in the condensed phase is obtained for the imposed mass flux by integrating Equations . The surface temperature is found from the pyrolysis law to verify the equability of the imposed mass flux and the surface regression rate defined by the pyrolysis law. The interface conditions for the gas phase are obtained via Equations and The mesh of the gas phase domain is automatically refined to limit the relative variation of the solution variables between each pair of adjacent cells and the relative variation of variable differences between three neighboring cells.

6. Pyrolysis Law

6.1. Parameters Choice

The overall combustion model can be broken down into three main founding blocks: the revised gas-phase kinetic model describing the reactions within the flame, the conformal condensed-phase reaction defining the gaseous species generated at the surface of the regressing propellant, and the pyrolysis law defining the dependance between the surface temperature and regression rate. The pyrolysis law has a significant effect on the stability of the coupled flame / solid model. The combustion of ammonium perchlorate can be unstable under certain conditions, independently of external acoustic disturbances. This is the so-called intrinsic combustion instability of the propellant. These phenomena were studied by Denison and Baum [40], then by Zel'dovich and Novozhilov [13].

The two studies, following different reasoning, result in the same stability limit. According to the Zel'dovich-Novozhilov (ZN) theory, this limit is characterized by sensitivity parameters from the steady-state combustion of the propellant. We define these parameters at constant pressure:

$$k = (T_s - T_0)\left(\frac{\partial \ln m}{\partial T_0}\right)_P \tag{20}$$

$$r = \left(\frac{\partial T_s}{\partial T_0}\right)_P \tag{21}$$

Where k and r are the sensitivity coefficients of the mass flux and surface temperature to the initial propellant temperature T_0. By introducing a small perturbation of the regression velocity and temperature field in the condensed phase and then linearizing the energy equation in the propellant, it is possible to obtain the stability condition:

$$r > r_L = \frac{(k-1)^2}{k+1} \tag{22}$$

We also define the temperature sensitivity coefficient of the propellant:

$$\sigma = \left(\frac{\partial \ln V_{\text{reg}}}{\partial T_0}\right)_P \tag{23}$$

When performing time-dependent simulations, it is important that the coupled combustion model is intrinsically stable. To this end, the pyrolysis law is designed making use of the ZN theory. Recalling the definition of the pyrolysis law, Equation (14), two constants need to be defined: the pre-exponential factor A, and the activation temperature T_a. It is to be noted that they are tunable parameters, and that multiple values can be found in the literature, see [7, 11]. The methodology described below is based on constraints to define the A and T_a parameters. A first constraint is to ensure stability of the coupled combustion model. Employing the ZN stability condition, Equation (22), the coupled combustion model will be stable up to pressure P if:

$$r = r_L \tag{24}$$

The values of r and r_L implicitly depend on the pressure and selected set (A, T_a). Performing coupled simulations for various values of (A, T_a), the sets verifying Equation (24) are found. These sets define curves $A = A_{min}(T_a, P)$, which are shown in Figure 12 for various pressures. A first constraint on the selection of (A, T_a) is then the stability condition at pressure P:

$$A > A_{min}(T_a, P) \tag{25}$$

For a selected activation temperature and a given pressure, if we choose $A > A_{min}(T_a, P)$ the model is stable at this pressure, inequality (25) providing the ZN stability condition $r > r_L$. With $A < A_{min}(T_a, P)$, the time-dependent solution would display an oscillatory instability. This can be explained by the existence of a minimal mass-flow rate, below which not enough energy is fed back from the flame to the burning propellant such as to maintain its regression. One can note that $A_{min}(T_a, P)$ increases with pressure: the stability constraint (25) becomes more stringent as pressure grows up.

When selecting the parameters (A, T_a) of the pyrolysis law, the stability condition $A > A_{min}(T_a, P)$ is not restrictive enough. Indeed, applying the stability contraint as described above, the activation temperature T_a is still a free parameter. To add more constraints, one can use Equation (14), which explicitly defines a relation between the surface temperature and regression rate:

$$T_s = \frac{T_a}{\ln\left(\frac{A}{\rho_c V_{reg}}\right)} \tag{26}$$

The parameters (A, T_a) should be chosen so that Equation (26) correlates with experimental data. The discrepancy between the analytical relation (26) and available experimental data points [2–4] can be assessed via the following L_2 error norm:

$$\delta_{err}(A, T_a) = \left[\frac{1}{N}\sum_{i=1}^{N}\left(T_s^i - \frac{T_a}{\ln\left(\frac{A}{\rho_c V_{reg}^i}\right)}\right)^2\right]^{\frac{1}{2}} \tag{27}$$

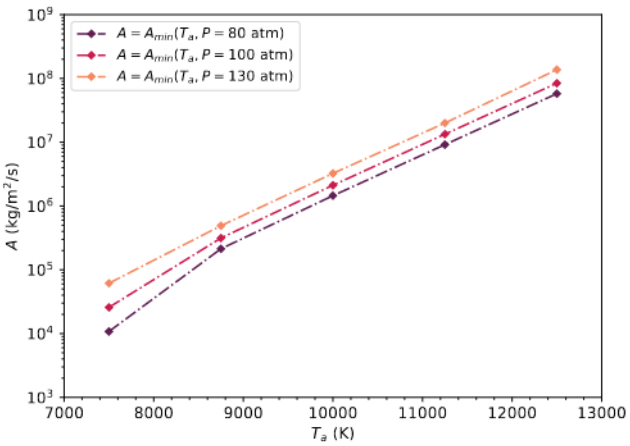

Fig. 12: Evolution $A = A_{min}(T_a, P)$ versus the activation temperature, for different pressures (80, 100 and 130 atm). Initial temperature of the solid AP: 298 K.

Where N is the number of experimental data points, and the i-th data point is $\left(V_{reg}^i, T_s^i\right)$.
The second constraint on the selection of (A, T_a) is then that this set of values is to minimize $\delta_{err}(A, T_a)$. For a selected activation temperature, we define $A^*(T_a)$ minimizing this deviation, as:

$$A^*(T_a) = \arg\left(\min_A \delta_{err}(A, T_a)\right) \tag{28}$$

The evolution of $\delta_{err}(A, T_a)$ versus A is presented in Figure 13 for various activation temperatures. With these curves, the values of $A^*(T_a)$ are determined and marked by points. The curves $T_s = f(V_{reg})$ obtained from the analytical relations $T_s(A^*(T_a), T_a)$, defined by Equation (26), are traced in Figure 14. Because of the large scatter of the experimental data points, the choice of T_a is not evident.

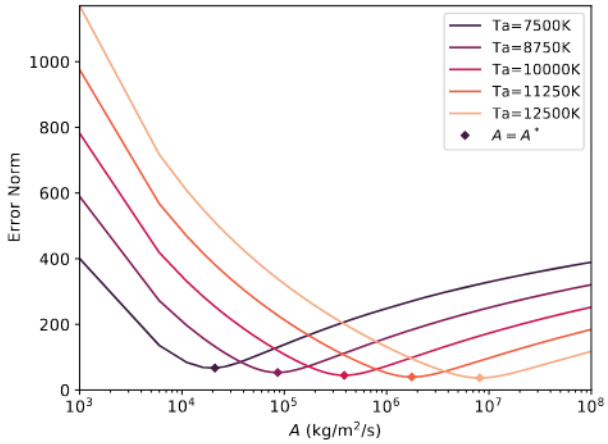

Fig. 13: Evolution of $\delta_{err}(A, T_a)$ with A for various activation temperatures, Equation (27).

In order to select the values of A and T_a, the curves $A = A_{min}(T_a, P)$ are plotted for various pressures, together with the curve $A = A^*(T_a)$, Figure 15. The selected set (A, T_a) must ensure the ZN stability of the coupled combustion model up to a high pressure. It must also provide results on $T_s(V_{reg})$ in agreement with the experimental data, *i.e.* A must be chosen close to $A^*(T_a)$. It is seen from Figure 15 that it is impossible to ensure the model stability up to 130 atm without using values of A which would deviate too much from $A^*(T_a)$. A good compromise is found selecting $A = 3 \cdot 10^4 \mathrm{kg/m^2/s}$ and $T_a = 7500\,\mathrm{K}$. These values ensure the stability of the coupled combustion model up to at least 100 atm, and providing a small value of $\delta_{err}(A, T_a)$.

6.2. Effect on Macroscopic Parameters

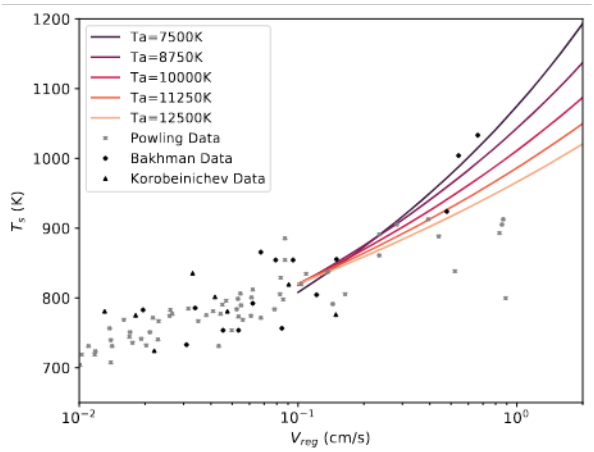

Fig. 14: Dependency between AP surface temperature and regression rate for various T_a and $A = A^*(T_a)$, Equation (26). Symbols: experiments [2–4]. Lines: computed relations.

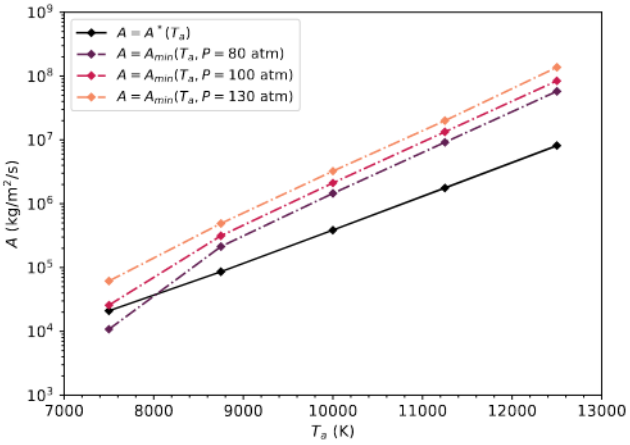

Fig. 15: Comparison of the curves $A = A_{min}(T_a, P)$ for different pressures (80, 100 and 130 atm), with the curve $A = A^*(T_a)$.

It is also of interest to study the effect of the pyrolysis law parameters on some macroscopic characteristics of the combustion: the regression rate V_{reg}, and surface temperature T_s. The modelling results are presented in Figure 16 for a pressure of 100 atm.

For a given activation temperature, the regression rate first increases as a function of the pre-exponential factor, as the heat feedback to the condensed phase increases with growing mass-flow rate; on the other hand, the surface temperature is steadily decreasing, following the direct relationship between A, T_a and V_{reg} provided by the pyrolysis law (26). At the maximum of regression rate, the pre-exponential factor reaches a critical value, above which the regression rate decreases slowly. At this point, the surface temperature becomes too low and chemical reactions are slowed down near the AP surface, hence reducing the heat feedback to the condensed phase. When this progressive phenomenon becomes apparent, the surface temperature is below 900 K for the considered pressure. The value of the regression rate maximum does not depend on the activation temperature, and is mainly controlled by the value of parameter α determining the overall thermal effect of the condensed phase decomposition. Depending on the activation temperature, the point $A = A_{min}(T_a, P = 100$ atm$)$ on the curve $V_{reg}(A)$ changes its location with respect to the maximum: it is on the left branch for $T_a = 7500$ K, at the maximum for $T_a = 8750$ K, and on the right branch for greater values of T_a.

The effect of the pyrolysis law parameters on the sensitivity coefficient σ is shown in Figure 17, for a pressure of 100 atm. The temperature sensitivity appears to be an increasing function of the pre-exponential factor A. The slope of the curve $\sigma(A)$ decreases with the activation temperature rise. Note that the value of σ for $A = A_{min}(T_a, P = 100$ atm$)$ depends on T_a within the lower part of the studied range and becomes stable at

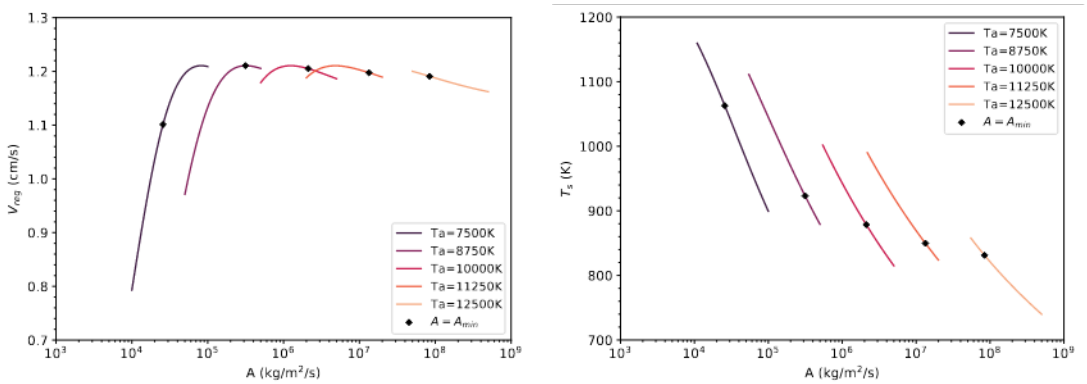

Fig. 16: Calculated regression rate (left) and surface temperature (right) versus pre-exponential factor for different activation temperatures. Ambient pressure 100 atm. Initial condensed-phase temperature 298 K.

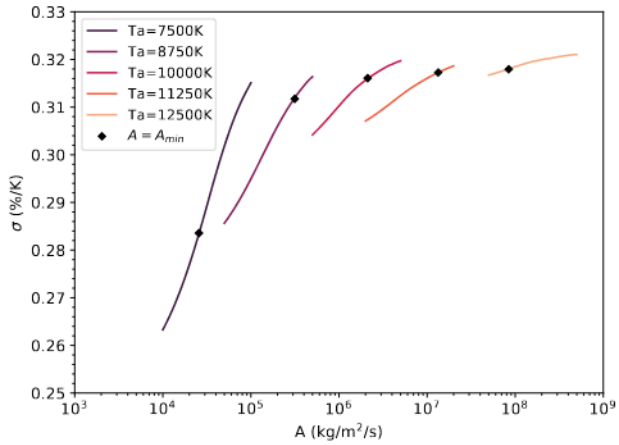

Fig. 17: Calculated sensitivity coefficient versus pre-exponential factor for different activation temperatures. Ambient pressure 100 atm. Initial condensed-phase temperature 298 K.

$T_a \geq 1000$ K.

7. AP Combustion Results

7.1. Ermolin's Flame

The coupled approach described above is first applied to the case of the low-pressure AP flame studied by Ermolin et al. [5] and Tereshenko et al. [6]. The species mole fraction profiles, obtained with the present model and with the Gross reference model, are compared with the experimental data for the main AP flame products and nitrogen-containing species, Figure 18.

The present model provides results in agreement with the experimental data. On the other hand, the Gross model appears to suffer from deficiencies, mainly for nitrogen-containing species. The N_2 level is over-predicted above the surface, and an important rise is observed around $x = 10^{-2}$ cm, whereas the experimental data shows a slight increase in N_2. The present model produces a significant amount of NO, whereas the Gross model predicts a low NO level within the flame. Hence, with this latter model, nitrogen-containing species are converted at an excessive rate to the final product N_2, without forming enough NO as an intermediate species.

The temperature profile computed with the present model is presented in Figure 19, and compared against the experimental data from Tereshchenko et al. [6]. The results obtained with the Gross model [10] and two more models from the literature (Smyth et al. [11], Meynet et al. [9]) are presented as well. Most modeling results are in good agreement with this experimental temperature profile, with the exception of the Gross model which significantly overestimates the flame temperature. Smyth and Meynet also used this temperature profile as a validation case in their modeling studies. The compared profiles differ mainly in the predicted surface temperature and the downstream behaviour. In the Meynet model, the surface temperature is fixed at 825 K resulting in a significantly

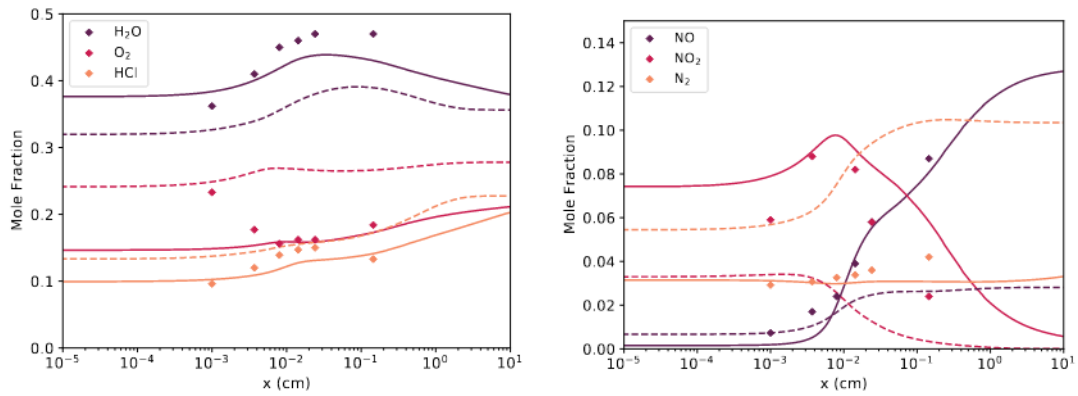

(a) Main products

(b) Main nitrogen-containing species

Fig. 18: Species profiles for the AP flame at 0.6 atm and initial temperature 533 K. Symbols: experiment [5]. Solid lines: present model. Dashed lines: Gross model [10].

higher temperature near the surface. The Smyth model profile is particularly distinguished by a second marked rise of temperature around $x = 1$ cm.

It is to be noted that this flame is the only AP combustion test case in the literature with available experimental profiles. Since the original publication from Ermolin et al. [5] in 1981, no significant progress has been made in the experimental characterisation of the AP flames. With a single available test case, a large variety of combustion models emerged over the years, each predicting more or less correctly the Ermolin flame, but with sometimes very different underlying physics. Experimental work on this matter, for instance at higher pressure, would be a great benefit for the solid propellant community.

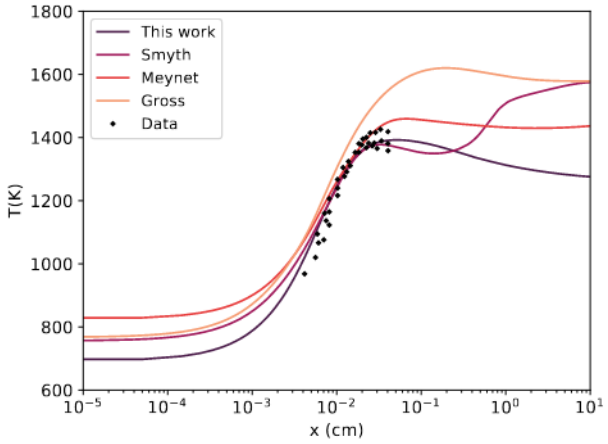

Fig. 19: Temperature profiles in the AP flame at 0.6 atm and initial temperature 533 K. Symbols: experiment [6]. Lines: model prediction.

The NO and N_2 profiles predicted with the different models are shown in Figure 20. The observed rapid conversion of NO into N_2 is due to the irreversible reaction $2NO \rightarrow N_2 + O_2$ in the Smyth model. The second temperature rise obtained with the Smyth model is caused by the energy released by this specific reaction. This reaction was introduced in order to decrease the NO level past the flame front, judged by Smyth et al. to be too far from the thermochemical equilibrium. Such an irreversible and non-elemental reaction appears to be artificial and destabilizes the equilibrium of the NO_x chemistry. The proposed model, whose NO_x chemistry has been previously validated on experimental cases, predicts a significant level of NO and reproduces the experimental points of [5]. These results suggest that NO may indeed be an important end product for the AP flame: thermochemical equilibrium could be reached far downstream of the flame front.

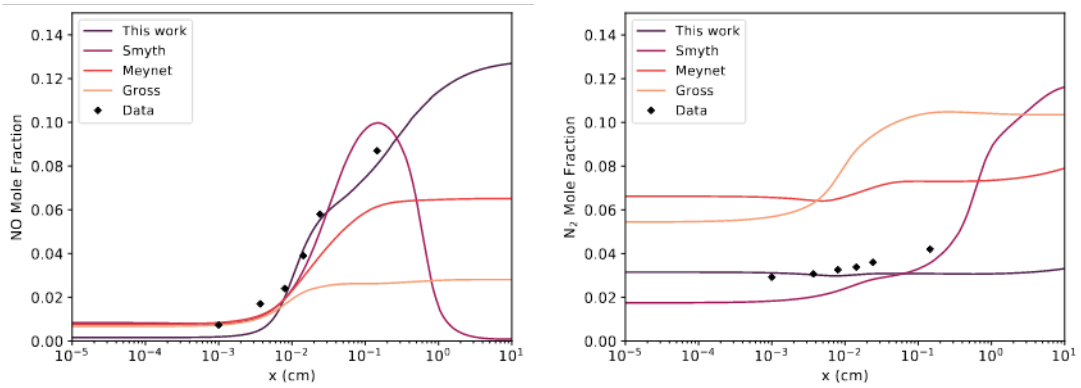

(a) NO mole fraction

(b) N_2 mole fraction

Fig. 20: Profiles of NO and N_2 in the AP flame at 0.6 atm and initial temperature 533 K. Symbols: experiment [5]. Lines: model prediction.

7.2. Macroscopic Combustion Parameters

The validity of the coupled model is further verified by computing macroscopic characteristics of AP combustion. The evolution of AP regression rate versus pressure is presented in Figure 21, or the four combustion models compared in the previous test case. Satisfying agreement is obtained between computed results and experimental data points, for all models. Indeed, they were all adjusted to fit these points. For a given gas-phase kinetic model, the condensed-phase decomposition model can be adapted to ensure sufficient heat production at the AP surface. The ratio α between the exothermic and endothermic decomposition pathways, Equation (13), has a first order effect on the regression rate and can be tuned to this end. With suitable formulation of the AP decomposition products and pyrolysis law, it is possible to obtain correct evolution of the regression rate with pressure for pure AP using quite different gas-phase mechanisms .On the other hand, gas-phase kinetics becomes critical when simulating the combustion of composite propellants: decomposition and combustion products of pure AP react with species produced by the pyrolysis of the binder. A diffusion flame formed near the AP/binder interface provides intense surface heating due to the additional heat release, thereby increasing the local regression rate. Therefore, a correct representation of the gas-phase kinetics within the AP flame is a necessary first step to accurately model the combustion of AP-based composite propellants.

The curves obtained with the different models can be approximated by a Vieille law of the form:

$$V_{\text{reg}} = aP^n \tag{29}$$

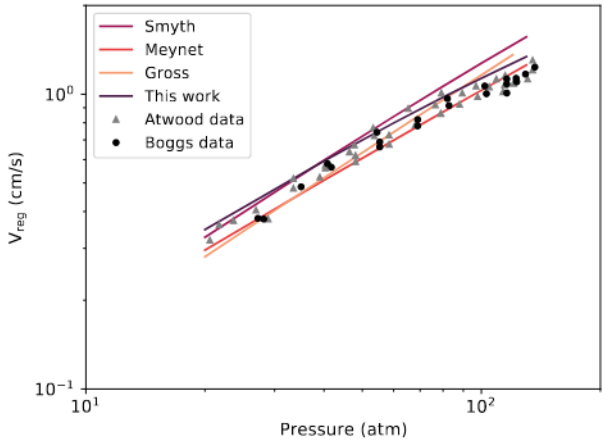

Fig. 21: AP regression rate as a function of pressure. Initial temperature 298 K. Symbols: experiments [1, 38]. Lines: model predictions.

Where V_{reg} is the regression speed and P is the ambient pressure. We note that n is independent of pressure for the

models of Gross, Meynet and Smyth. In the case of the present model, n decreases with pressure. This behaviour is consistent with the experimental results: the AP regression rate curve exhibits a decrease in its slope at high pressure. Thus, while the Smyth model slightly overestimates the measured regression rate at pressures higher than 80 atm, the present model observes the experimental trend other the whole pressure range. This behaviour of the present model is a consequence of the choice of the pyrolysis law. Looking at Figure 16, the design point for the current model is located in the steep region of the curve $V_{\mathrm{reg}}(A)$ for $P = 100$ atm. The regression rate tends to move farther from the maximum value achievable with increasing pressure, explaining the variability of n.
The evolution of the AP surface temperature with the regression rate is shown in Figure 22. The Meynet model assumes the surface temperature to be independent of the regression rate and equal to the melting temperature of AP (825 K in this model). This assumption appears to be too simplifying in view of the higher surface temperatures experimentally observed. The curve produced by the present model is above the Smyth model curve for high regression rates, but still indicates acceptable temperatures considering the large scatter in the experimental data in this range of regression rate.

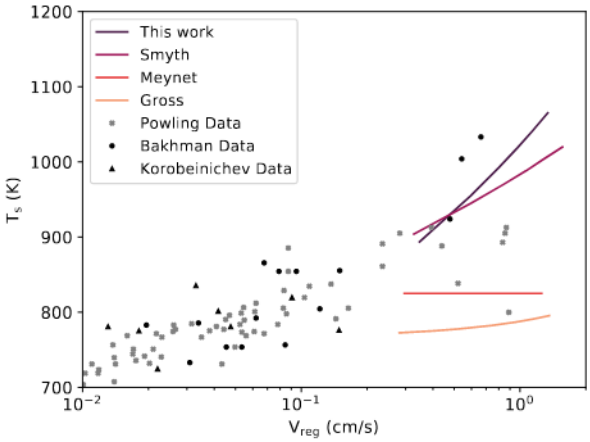

Fig. 22: AP surface temperature as a function of regression rate. Initial temperature 298 K. Symbols: experiments [2–4]. Lines: model prediction.

The parameters k and r have been calculated according to the ZN theory, Equation (20). The model of Meynet is not included in this analysis, as it assumes a fixed surface temperature. The Gross model isn't considered as well, as it uses separate correlations for the surface temperature and regression rate with respect to the surface heat flux, which is not a good approach for unsteady simulations. Both models are stable at low pressure and approach the stability limit as the pressure increases. In order to characterize more precisely the stability limit of the two models, the evolution with pressure of the stability margin $r - r_L$ is plotted in Figure 23. The combustion becomes unstable following an oscillatory regime below the zero level. The Smyth model becomes unstable around 87.5 atm, while the present model is stable up to 105 atm, as predicted when designing the pyrolysis law. This increased stability range is of practical interest, allowing unsteady calculations to be performed over a broader range of pressure.
The trends of the temperature sensitivity $\sigma(P)$ for the different models considered are plotted in Figure 24. They are compared to the experimental data of Atwood et al. [1]. It is observed that the experimental trend is not captured by the models, as they predict a nearly constant temperature sensitivity over the studied pressure range. The present model predictions are at the upper boundary of the experimental data points scatter.

8. Conclusion

Using recent research by Shrestha et al. [12] and Pelucchi et al. [18], a revised gas-phase mechanism for AP combustion has been elaborated. This new mechanism produces satisfactory results for simple reactive systems, allowing validation of its main sub-mechanisms. The test cases also revealed deficiencies in the reference model from Gross et al. [10]: this mechanism was never validated on fundamental data, yet managed to reproduce the available macroscopic experimental data on AP combustion. This work highlights the importance of the validation process when assembling a complex gas-phase mechanism: as testing macroscopic combustion characteristics (*e.g.* regression rate) cannot reveal possible deficiencies in the temperature and species profiles. But when trying to simulate the combustion of composite propellants, interactions between species from different ingredients would be very sensitive to the local conditions in the flame. A conformal condensed-phase decomposition model has been designed for the revised kinetic mechanism, including the gaseous product composition and an adapted

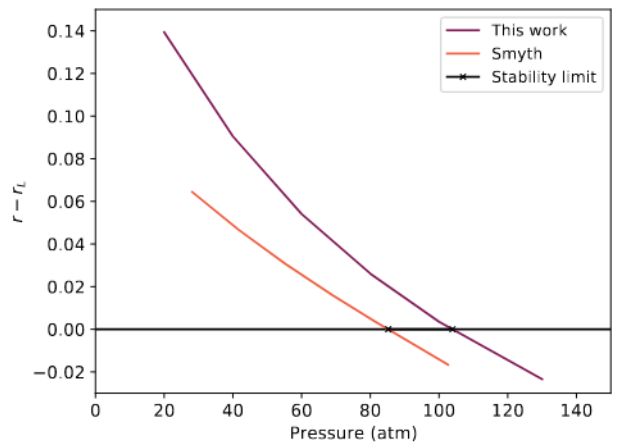

Fig. 23: Stability limit according to the ZN theory for different models.

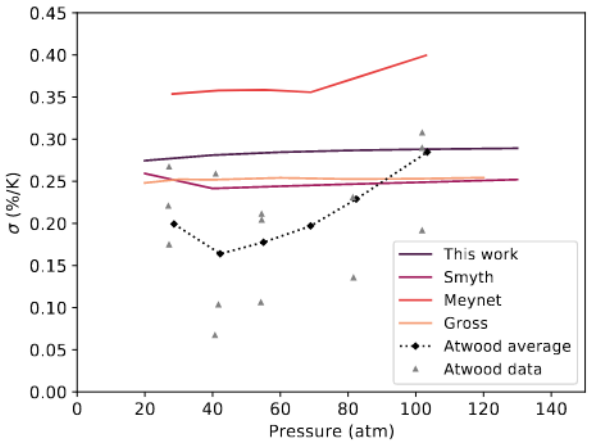

Fig. 24: Temperature sensitivity as a function of pressure. Symbols: experiment [1]. Lines: models [9–11].

pyrolysis law. The pyrolysis law parameters have been chosen ensuring combustion models stability up to 100 atm. The resulting coupled model has been validated on the case of the low-pressure AP flame studied by Ermolin et al. [5] and Tereshenko et al. [6]. The profiles of the main species molar fraction and the temperature profile obtained are in good agreement with the available experimental data. The macroscopic characteristics of AP combustion (surface temperature, regression rate) were evaluated at different pressures. The regression rate shows a pressure dependence of the form aP^n with n decreasing with pressure. This result is consistent with experimental trend and represents a specificity of the new model compared to other reference models. A Zel'dovich-Novozhilov stability study was performed at variable pressure. The model is intrinsically stable up to 105 atm, allowing for unsteady simulation to be performed over a wide range of pressure. The evolution of the temperature sensitivity coefficient agrees with the experimental data.

9. Acknowledgments

The authors would like to thank Direction Générale de l'Armement and ONERA for funding and supporting the present work.

References

[1] A. I. Atwood, T. L. Boggs, P. O. Curran, T. P. Parr, D. M. Hanson-Parr, C. F. Price, J. Wiknich, Burning rate of solid propellant ingredients, part 1: Pressure and initial temperature effects, J. Propul. Power 15 (1999) 740–747.

[2] N. N. Bakhman, Y. S. Kichin, S. M. Kolyasov, A. E. Fogelzang, Investigation of the thermal structure of the burning zone in condensed mixtures by fine thermocouples, Combust. Flame 26 (1976) 235–247.

[3] J. Powling, Experiments relating to the combustion of ammonium perchlorate-based propellants, Symp. (Int.) Combust. 11 (1967) 447–456.
[4] O. P. Korobeinichev, A. A. Zenin, A. G. Tereshchenko, V. M. Puchkov, Investigation of the structure of a combustion wave of mixed systems based on apc, pmma, and a catalyst using mass-spectrometric and thermocouple methods, Combust., Explo. Shock. 13 (1977) 273–279.
[5] N. E. Ermolin, V. M. Fomin, O. P. Korobeinichev, A. G. Tereshchenko, Measurement of the concentration profiles of reacting components and temperature of an ammonium perchlorate flame, Combust., Explo. Shock. 18 (1982) 36–38.
[6] A. G. Tereshchenko, O. P. Korobeinichev, Correctness of mass-spectrometric probe measurements when investigating the flame structure of condensed systems, Combust., Explo. Shock. 18 (1983) 645–650.
[7] M. Tanaka, M. Beckstead, A three-phase combustion model of ammonium perchlorate, 32nd Joint Propulsion Conference and Exhibit, 1996, p. 2888.
[8] Q. Jing, M. Beckstead, M. Jeppson, Influence of AP solid-phase decomposition on temperature profile and sensitivity, 36th AIAA Aerospace Sciences Meeting and Exhibit, 1998, p. 448.
[9] N. Meynet, Simulation numérique de la combustion d'un propergol solide, Ph.D. thesis, Université Paris VI (2005).
[10] M. L. Gross, Two-dimensional modeling of AP/HTPB utilizing a vorticity formulation and one-dimensional modeling of AP and ADN, Ph.D. thesis, Brigham Young University (2007).
[11] D. A. Smyth, Modeling solid propellant ignition events, Ph.D. thesis, Brigham Young University (2011).
[12] K. P. Shrestha, L. Seidel, T. Zeuch, F. Mauss, Detailed kinetic mechanism for the oxidation of ammonia including the formation and reduction of nitrogen oxides, Energ. Fuel. 32 (2018) 10202–10217.
[13] B. V. Novozhilov, Theory of nonsteady burning and combustion stability of solid propellants by the Zeldovich-Novozhilov method, in: Nonsteady Burning and Combustion Stability of Solid Propellants, American Institute of Aeronautics and Astronautics, 1992, pp. 601–641.
[14] K. P. Shrestha, C. Lhuillier, A. A. Barbosa, P. Brequigny, F. Contino, C. Mounaïm-Rousselle, L. Seidel, F. Mauss, An experimental and modeling study of ammonia with enriched oxygen content and ammonia/hydrogen laminar flame speed at elevated pressure and temperature, Symp. (Int.) Combust 38 (2021) 2163–2174.
[15] J. B. Baker, R. K. Rahman, M. Pierro, J. Higgs, J. Urso, C. Kinney, S. Vasu, Experimental ignition delay time measurements and chemical kinetics modeling of hydrogen/ammonia/natural gas fuels, J. Eng. Gas. Turb. Power 145 (2023) 041002.
[16] M. D. Smooke, R. A. Yetter, T. P. Parr, D. M. Hanson-Parr, M. A. Tanoff, M. B. Colket, R. J. Hall, Computational and experimental study of ammonium perchlorate/ethylene counterflow diffusion flames, Proc. Combust. Inst. 28 (2000) 2013–2020.
[17] N. E. Ermolin, Model for chemical reaction kinetics in perchloric acid-ammonia flames, Combust., Explo. Shock. 31 (1995) 555–565.
[18] M. Pelucchi, A. Frassoldati, T. Faravelli, B. Ruscic, P. Glarborg, High-temperature chemistry of HCl and Cl2, Combust. Flame 162 (2015) 2693–2704.
[19] D. G. Goodwin, R. L. Speth, H. K. Moffat, B. W. Weber, Cantera: An object-oriented software toolkit for chemical kinetics, thermodynamics, and transport processes (2021). doi:https://doi.org/10.5281/zenodo.4527812.
[20] O. Mathieu, E. L. Petersen, Experimental and modeling study on the high-temperature oxidation of ammonia and related nox chemistry, Combust. Flame 162 (2015) 554–570.
[21] A. Hayakawa, T. Goto, R. Mimoto, Y. Arakawa, T. Kudo, H.Kobayashi, Laminar burning velocity and markstein length of ammonia/air premixed flames at various pressures, Fuel. 159 (2015) 98–106.
[22] V. F. Zakaznov, L. A. Kursheva, Z. I. Fedina, Determination of normal flame velocity and critical diameter of flame extinction in ammonia-air mixture, Combust., Explo. Shock. 14 (1978) 710–713.
[23] U. J. Pfahl, M. C. Ross, J. E. Shepherd, K. O. Pasamehmetoglu, C. Unal, Flammability limits, ignition energy, and flame speeds in H2–CH4–NH3–N2O–O2–N2 mixtures, Combust. Flame 123 (2000) 140–158.
[24] P. D. Ronney, Effect of chemistry and transport properties on near-limit flames at microgravity, Combust. Sci. Technol. 59 (1988) 123–141.
[25] T. Jabbour, D. F. Clodic, Burning velocity and refrigerant flammability classification, ASHRAE Tran. 110 (2004) 522.
[26] K. Takizawa, A. Takahashi, K. Tokuhashi, S. Kondo, A. Sekiya, Burning velocity measurements of nitrogen-containing compounds, J. Hazard. Mater. 155 (2008) 144–152.
[27] G. Dayma, P. Dagaut, Effects of air contamination on the combustion of hydrogen-effect of NO and NO2 addition on hydrogen ignition and oxidation kinetics, Combust. Sci. Technol. 178 (2006) 1999–2024.
[28] O. Mathieu, A. Levacque, E. Petersen, Effects of no2 addition on hydrogen ignition behind reflected shock waves, Symp. (Int.) Combust 34 (2013) 633–640.
[29] A. Lifshitz, P. Schechner, The mechanism of the H2+ CL2 reaction: ignition behind reflected shocks, Int. J. Chem. Kinet. 7 (1975) 125–142.
[30] J. C. Leylegian, H. Y. Sun, C. K. Law, Laminar flame speeds and kinetic modeling of hydrogen/chlorine combustion, Combust. Flame 143 (2005) 199–210.
[31] S. Rahman, V. Giovangigli, V. Borie, Pressure and initial temperature sensitivity coefficient calculations in ammonium perchlorate flames, J. Propul. Power 27 (2011) 1054–1063.
[32] R. J. Kee, F. M. Rupley, E. Meeks, J. A. Miller, Chemkin-II: A FORTRAN chemical kinetics package for the analysis of gas-phase chemical and plasma kinetics, Tech. Rep. SAND-89-8009, Sandia National Laboratories, Livermore, CA, USA (5 1989).
[33] A. Ern, V. Giovangigli, Multicomponent Transport Algorithms, Vol. 24, Springer Science & Business Media, 1994.
[34] A. Ern, V. Giovangigli, Fast and Accurate Multicomponent Transport Property Evaluation, J. Comput. Phys. 120 (1995) 105–116.
[35] L. R. Petzold, Description of DASSL: a differential/algebraic system solver, Tech. Rep. SAND-82-8637, Sandia National Laboratories, Livermore, CA, USA (1982).

[36] M. W. Chase, NIST-JANAF Thermochemical Tables, 4th Edition, American Institute of Physics, 1998.
[37] D. M. Hanson-Parr, T. P. Parr, Thermal properties measurements of solid rocket propellant oxidizers and binder materials as a function of temperature, J. Energ. Mater. 17 (1999) 1–48.
[38] T. L. Boggs, Deflagration rate, surface structure, and subsurface profile of self-deflagrating single crystals of ammonium perchlorate, AIAA J. 8 (1970) 867–873.
[39] C. Guirao, F. A. Williams, A model of ammonium perchlorate deflagration between 20 and 100 atm, AIAA J. 9 (1971) 1345–1356.
[40] M. R. Denison, E. Baum, A simplified model of unstable burning in solid propellants, ARSJ-Am Rocket Soc J. 31 (1961) 1112–1122.